



Chiral Perovskite Nanocrystal Growth inside Helical Hollow Silica Nanoribbons

Peizhao Liu, Yann Battie, Takaki Kimura, Yutaka Okazaki, Piyanan Pranee, Hao Wang, Emilie Pouget, Sylvain Nlate, Takashi Sagawa, Reiko Oda

► To cite this version:

Peizhao Liu, Yann Battie, Takaki Kimura, Yutaka Okazaki, Piyanan Pranee, et al.. Chiral Perovskite Nanocrystal Growth inside Helical Hollow Silica Nanoribbons. *Nano Letters*, 2023, 23 (8), pp.3174-3180. 10.1021/acs.nanolett.2c04823 . hal-04274067

HAL Id: hal-04274067

<https://hal.science/hal-04274067>

Submitted on 8 Nov 2023

HAL is a multi-disciplinary open access archive for the deposit and dissemination of scientific research documents, whether they are published or not. The documents may come from teaching and research institutions in France or abroad, or from public or private research centers.

L'archive ouverte pluridisciplinaire **HAL**, est destinée au dépôt et à la diffusion de documents scientifiques de niveau recherche, publiés ou non, émanant des établissements d'enseignement et de recherche français ou étrangers, des laboratoires publics ou privés.

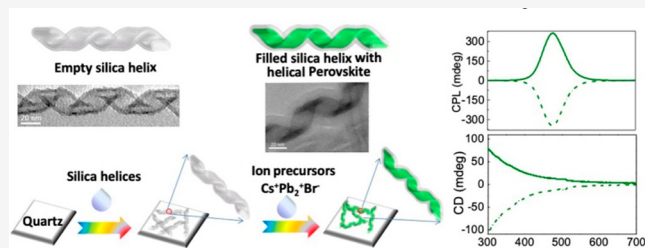
Chiral Perovskite Nanocrystal Growth inside Helical Hollow Silica Nanoribbons

Peizhao Liu, Yann Battie, Takaki Kimura, Yutaka Okazaki, Piyanan Pranee, Hao Wang, Emilie Pouget, Sylvain Nlate, Takashi Sagawa, and Reiko Oda*

ABSTRACT: Helical perovskite nanocrystals (H-PNCs) were prepared using nanometric silica helical ribbons as platforms for the in situ growth of the crystals using the supersaturated recrystallization method. The H-PNCs grow inside nanometric helical porous silica, and their handedness is determined by the handedness of porous silica templates. They show both strong induced circular dichroism (CD) and strong induced circularly polarized luminescence (CPL) signals, with high dissymmetry g-factors. Right-handed and left-handed PNCs show respectively positive and negative CD and CPL signals, with a dissymmetry g-factor (abs and lum) of $\sim \pm 2 \times 10^{-2}$. Simulations based on the boundary element method demonstrate that the circular dichroism originates from the chiral shape of H-PNCs.

KEYWORDS: Silica nanohelices, perovskite nanocrystals, chiral shape, circular dichroism, circularly polarized luminescence

Perovskite materials attract a lot of attention due to their outstanding optoelectronic properties and promising applications, such as solar cells and light-emitting diodes (LEDs). The lower trap densities¹ and long carrier-diffusion length² have led to the solar cells with efficiency up to 20%;³ the higher photoluminescence quantum yields and tunable emission have enabled high-performance LEDs.⁴ Among various semiconductor nanocrystals, optically active (OA) ones are of particular interest, which can show strong circular dichroism (CD) and circularly polarized luminescence (CPL) signals,⁵ second-harmonic generation (SHG),⁶ piezoelectricity, pyroelectricity,⁷ ferroelectricity,⁸ and topological quantum properties.⁹ The distinctive properties result in many potential and promising applications in chirophotoelectronics, such as CPL detector,¹⁰ circularly polarized LEDs,¹¹ 3D display,¹² quantum computing,¹³ quantum communication,¹⁴ and spintronics.^{15–19} The preparation of chiral perovskite materials therefore represents a particularly hot topic. Several review papers have described the ways to endow chirality to perovskite materials and their potential and promising applications.^{16,20–22} The chirality generation in nanocrystals (NCs) can be roughly classified into four approaches: a) coordination of chiral ligands around NCs;^{23–25} b) chiral self-organization of NCs;^{26–28} c) chiral lattice;^{29,30} and d) chiral shape.^{31–33} The chiral ligands coordinated to the perovskite NCs can induce chiral distortion of the inorganic surface or chiral patterning of the surface ligands, and the electronic coupling between the chiral organic molecules and the inorganic structure results in optically active properties with



a dissymmetric g-factor of $\sim 10^{-3}$.¹⁶ The chirality endowed to perovskite NCs by inorganic^{26,27} or organic²⁸ templates has also been reported giving the similar order of g-factor. Chiral organic ammonium cations could be incorporated into the perovskite lattice which results in a chiral lattice of an organic inorganic hybrid perovskite structure forming 1D and 2D structures with a higher g-factor up to 10^{-2} .²¹ In order to obtain chiral perovskite NCs with higher g-factors, perovskite NCs having a chiral shape would be an alternative approach. Indeed, recently there have been some reports of chiral shaped NCs, and the mechanism of the formation is attributed to the differential growth rates of chiral facets possibly mediated by the presence of chiral ligands^{33–36} or the intrinsic chiral crystal structure.^{37,38} Another proposed mechanism is that the nuclei of the crystals contain screw dislocations which create a more reactive crystal growth front.^{39–43} Such screw-dislocation-mediated growth yields a helical or twisted shape. The growth of nanomaterials such as CdSe,⁴⁴ CdS,^{45,46} and InP⁴⁷ inside hollow structure materials^{48–50} was also reported. PNCs such as hybrid $\text{CH}_3\text{NH}_3\text{PbBr}_3$ ⁵¹ and inorganic CsPbX_3 ($X = \text{Cl}, \text{Br}, \text{I}$ or their mixture)^{52–54} were shown to grow inside the hollow materials with high luminescence due to their halide self-

Received: December 8, 2022

Revised: April 7, 2023

Published: April 13, 2023

passivation⁵⁵ and defect tolerance.⁵³ Meanwhile, so far, there is no report on clearly morphologically helical/twisted shaped perovskite NCs and the resulting chirality induction.

Inspired by these observations, we prepared helical PNCs. Their growth is assisted by the hollow silica ribbons via supersaturated recrystallization methods. The solution of ion precursors of perovskite was drop-casted on a surface on which the left-/right-handed hollow helical silica ribbons have first been deposited. During the solvent evaporation, the perovskite NCs grow in the hollow inner space of left- or right-handed chiral shape. These H-PNCs obtained with this very simple method show strong CD and CPL mirror images with a dissymmetry g-factor up to 2×10^{-2} which is much higher than the previously reported values from the chiral perovskite NCs (in the range of 10^{-3}). It should be noted that in the whole process of crystallization, no chiral ligands are used. The formation of chiral shaped H-PNCs originates solely from the confined crystallization of the ions in the hollow silica ribbons.

As previously reported, right- or left-handed silica nanohelices were synthesized using cationic bis-quaternary ammonium gemini surfactants of chemical formula $C_2H_4\text{-}1,2\text{-}((CH_3)_2N^+C_{16}H_{33})_2$, noted hereafter 16–2–16, which self-assemble in water to form nanometric helical structures in the presence of tartrate counterions. With L tartrate, 16–2–16 formed right-handed helices, and with D tartrate, left-handed helices are formed.^{56,57} The resulting nanohelices were used as templates for the sol–gel condensation of tetra-alkoxysilane to obtain silica nanohelices.^{58,59} The organic template Gemini-L/D-tartrate was washed away leaving helical pores inside the silica helices. Tip-sonication was used to cut the helices and to obtain a homogeneous suspension in ethanol. Using these porous silica nanohelices as templates, two methods were developed to obtain the H-PNCs as shown in Figure 1. The two-step method is to first drop-cast the suspension of porous silica helices. When a film of dried deposition of helices is obtained, a DMF solution of a stoichiometric mixture of ion precursors (SI) is drop-casted on the film. For the one step method, the various amounts of hollow silica helical ribbons were mixed with the solution of ion precursors in DMF, the suspension was drop-casted on a quartz substrate, and DMF was dried to obtain a film. With both methods, upon solvent evaporation, and the increased concentration of the ion mixture with much higher electron density (higher contrast), domains are observed inside the silica helical ribbons forming helical structures due to the supersaturated recrystallization.

We then investigated the optimal conditions to obtain the highest chiroptical signals by varying the parameters such as the relative concentration of ions/silica helices and temperature during the drying. For 1 mg of silica helical ribbons, the volume of hollow helical space is estimated as $2.84 \times 10^{-4} \text{ cm}^3$, as shown in Scheme (SI) and Table S1. If this volume is filled with CsPbBr_3 PNCs (4.42 g/mL), this would correspond to 1.25 mg of PNCs of 54 μL of ion precursors.

For the H-PNCs obtained by the two-step method, different quantities of silica helical ribbon suspension in ethanol (10 μg , 20 μg , 50 μg , 100 μg , and 200 μg) were first drop-casted and dried on the surface of the quartz slide at room temperature. Then, 10 μL of the above-mentioned ion precursor solution (230 μg) in DMF was drop-casted and allowed to dry at room temperature. This corresponds to the weight ratios of $\text{Cs}^+\text{Pb}^{2+}\text{Br}^-$ /silica helices of 23, 11.5, 4.6, 2.3, and 1.15. Considering our calculation on the weight ratio of ion precursors to inner helical space of silica ribbons of 1.25 for

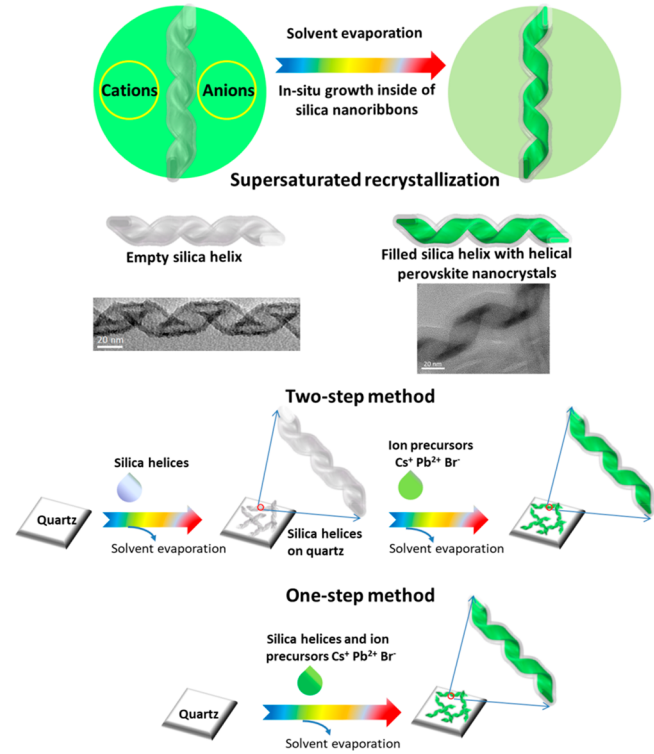


Figure 1. Scheme of the H-PNC growth inside the hollow silica helical ribbons through one-step or two-step drop casting methods and the TEM images of empty and PNC filled silica helices.

the fully filled helices, for most of these samples, the ions are in large excess. Such helical crystalline structures show UV–vis (first absorption peak at 508 nm) and fluorescence (ex @365 nm) spectra which correspond to the typical signals obtained from perovskite nanocrystals.⁶⁰ These helices also show remarkably strong induced CD and CPL signals, the signs of which depend on the handedness of the helices (Figure 2): the PNC with left-handed (right-handed) silica helical ribbons shows negative (positive) CD and CPL signals, respectively. The CD and CPL were measured with two azimuth angles at 0° and 90°, respectively, and accumulated to minimize the LD effect. Both CD-Abs and CPL-PL increases with lower $\text{Cs}^+\text{Pb}^{2+}\text{Br}^-$ /silica helices ratios, indicating the increase in the quantity of chiral PNCs inside silica helices with respect to the achiral ones outside the helices.

Detailed observation of these dark domains with high resolution TEM (HRTEM) shows that they are inside the pore of the silica helices replacing washed away gemini surfactants (Figure 2(e)). The average dimension of these helices is around 23 nm wide and 60 nm pitch, in good agreement with the size of the inner pore of the silica helices.^{61,62} To further investigate the nature of these helical dark domains specifically, the electron diffraction method was carried out. Although the helical dark domains are very small (Figure 2f), the selected area electron diffraction (SAED) technique allows us to target the helical and crystal dark domains inside the silica helices while avoiding the contamination from the crystal information on the materials produced outside of silica helices. The selected area electron diffraction (SAED) pattern was clearly observed (Figure 2f) from the red circle area in Figure S2(a). Since silica nanohelices are amorphous structures, the observed SAED pattern indicates that the helical dark domain is composed of crystalline structures. The observed spots,

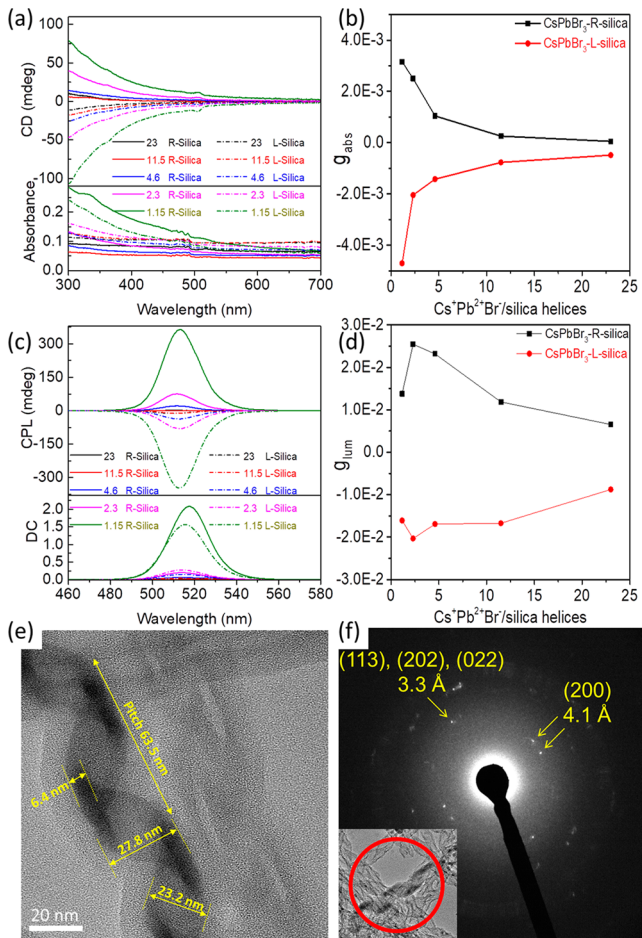


Figure 2. (a) CD, absorption and (c) CPL, DC (ex@365 nm) spectra of CsPbBr_3 -R/L-silica helices grown at different ratios of $\text{Cs}^+\text{Pb}^{2+}\text{Br}^-$ /silica helices for a given quantity of ions (230 μg , 10 μL of 0.04 M). The multiple peaks seen in the absorbance between 470 and 495 nm are the noise due to the light source of the CD apparatus. Corresponding (b) g_{abs} at 504 nm and (d) g_{lum} at 514 nm (ex @ 365 nm) variation for the different ratios of $\text{Cs}^+\text{Pb}^{2+}\text{Br}^-$ /silica helices. Both CD-Abs and CPL-PL increase with lower $\text{Cs}^+\text{Pb}^{2+}\text{Br}^-$ /silica helices ratios. (e) HRTEM image and (f) SAED pattern of CsPbBr_3 -R-silica helices (inset shows the domain of the sample observed with SAED).

corresponding to 4.1 and 3.3 \AA , are attributed to the (200) plane and (113), (202), and/or (022) planes of the orthorhombic phase of the CsPbBr_3 perovskite nanocrystal, respectively. These results support the existence of the CsPbBr_3 perovskite structure in the helical dark domains. As shown in Figures 5 and S6, even in the saturation conditions ($\text{Cs}^+\text{Pb}^{2+}\text{Br}^-$ /silica helices > 1.25), the PNCs grew only in part of the silica helices.

The importance of the nanospace of silica helices for perovskite crystallization was clearly demonstrated by the strong increase of the fluorescence in the presence of silica helices compared to the substrates on which the CsPbBr_3 ion mixture is deposited alone in the absence of silica helices (Figure 2c, Figures S3 and S4). The solution of the CsPbBr_3 ion mixture was drop-casted on bare quartz substrates in the presence of various quantities of helical hollow silica nanoribbons ($\text{Cs}^+\text{Pb}^{2+}\text{Br}^-$ /silica helices: 11.5, 4.6, 2.3, and 1.15, and no silica helices) and irradiated by UV light (@365 nm). In the absence of silica helices, extremely weak

fluorescence was observed, whereas a clear increase of the fluorescence was observed in the presence of the helices. The fluorescence property of H-PNCs was quantitatively evaluated by studying the photoluminescence quantum yield (PLQY). The internal and external PLQY were 3.9% and 0.8%, respectively. Such low values of PLQY compared with other CsPbBr_3 PNCs^{52–54} might be due to the weak emission of PNCs outside silica on the film. The emission intensity from the H-PNC film under UV light is bright enough to be observed by the naked eye (Figure S3). We have also observed that silica helices play an important role for the stability of the PL intensity. PL intensity of the H-PNC film was stable at least during 3 months even when the sample was kept under room light, humidity, and temperature (Figure S5).

The PNC helices show g_{abs} (\propto normalized CD signals by absorbance) $\sim 4 \times 10^{-3}$ for $\text{Cs}^+\text{Pb}^{2+}\text{Br}^-$ /silica helices = 1.15 and show an exponential decrease with the increasing $\text{Cs}^+\text{Pb}^{2+}\text{Br}^-$ /silica helices ratio. Interestingly g_{lum} (\propto normalized CPL signals by fluorescence) is globally much higher, $\sim 2 \times 10^{-2}$ for the $\text{Cs}^+\text{Pb}^{2+}\text{Br}^-$ /silica helices ratio around 2.3, and decreased more slowly with the increasing $\text{Cs}^+\text{Pb}^{2+}\text{Br}^-$ /silica helices ratio. This is probably because the proportion of achiral and larger NCs which forms outside the helices (Figure S3, S6) with respect to the chiral PNCs inside the helices increases with the decreasing quantity of silica ribbons. While both achiral and chiral NCs show similar absorbance but only chiral NCs show the CD signal, the achiral NCs show weaker fluorescence (FL) and no CPL signal. Only the PNCs inside the silica helical ribbons show both CPL and FL signals due to the confined size and surface passivation of the latter. Therefore, $g_{lum} \propto \text{CPL}_{\text{chiral PNCs}} / (\text{FL}_{\text{chiral PNCs}} + \text{FL}_{\text{achiral PNCs}}) \approx \text{CPL}_{\text{chiral PNCs}} / \text{FL}_{\text{chiral PNCs}}$ (outside achiral PNCs show weak luminescence) and $g_{abs} \propto \text{CD}_{\text{chiral PNCs}} / (\text{Abs}_{\text{chiral PNCs}} + \text{Abs}_{\text{achiral PNCs}})$. With a decreasing relative quantity of hollow silica helical ribbons, more NCs (absorbing but nonfluorescent) grow outside the hollow silica. This may explain why globally $g_{lum} > g_{abs}$ and also why g_{abs} decreases more drastically than g_{lum} with increasing the $\text{Cs}^+\text{Pb}^{2+}\text{Br}^-$ /silica helices ratio.

The extinction cross-section and the CD signals of helical PNCs were simulated using the boundary element method.⁶³ This method solves the Maxwell's equations for a complex interface which separates homogeneous isotropic medium. In our case, we consider two interfaces. The first one separates the air and the silica shell, while the second one separates the silica shell and the PNC cores. The dimensions of the structure are given in the scheme (SI). The height, thickness, width, diameter, and the pitch of the helical structure are 300 nm, 6 nm, 17 nm, 27, and 60 nm, respectively, as observed from the TEM images. The dielectric function of the silica shell is taken from the Palik handbook,⁶⁴ while the dielectric function of PNC comes from ref 65. The incident wave vector is perpendicular to the helix axis. Figure 3b shows the simulated extinction, scattering, and absorption cross section. For unpolarized incident light, left-handed H-PNC exhibits the same optical response as right-handed H-PNC. The absorption cross section is equal to 0 for a wavelength higher than 550 nm i.e. the band gap of PNC. However, due to the scattering effect, the extinction cross section does not vanish. A band centered at 517 nm is clearly observed in the absorption and extinction cross section spectra of H-PNC. This band is assigned to the resonant transition between the valence and conduction bands of PNC.

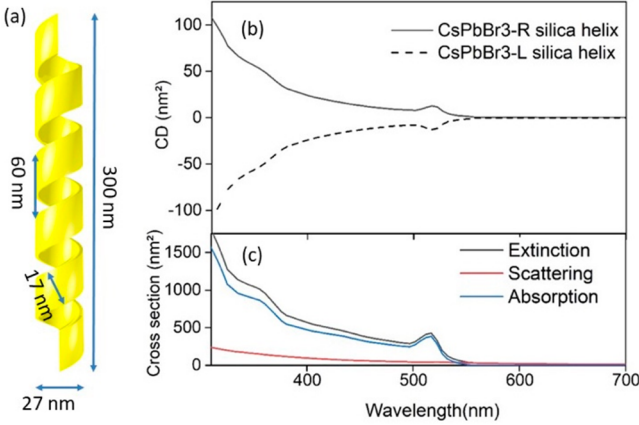


Figure 3. (a) Dimension of the PNC helix used for the simulation. (b) Simulated circular dichroism of H-PNCs. (c) Extinction, absorption, and scattering cross sections of H-PNC simulated by the boundary element method for unpolarized incident light.

The simulated CD signals, evaluated from the difference between the extinction cross sections simulated for left- and right-handed circular polarizations, are depicted on Figure 3b. They are in agreement with the measured ones in terms of their shapes and their signs depending on the handedness of the helices, confirming that this signal is related to the chiral shape of H-PNC. The CD intensity decreases with the increasing wavelength. It exhibits a band centered at 517 nm, i.e. the same wavelength as the resonant transition of electrons in PNC. According to Figure 3b, the small CD value observed above the band gap of PNC is related to the scattering effect. Such scattering (and chiral scattering) contribution was again confirmed experimentally using diffusion reflection CD (DRCD) measurements (Figure S10). However, both experimental signals and simulation unambiguously show that the absorbance and the absorbance based circular dichroism are the major contribution of the signals.

The crystallization of the PNCs inside the hollow silica helical ribbons is also affected by the solvent evaporation speed. As shown in Figure 4, the PNCs grown at lower temperatures (6.8 and 20 °C) show higher values of g_{abs} than those grown at higher temperatures (35 and 50 °C). TEM images (Figure 5) show that at high temperatures, larger and achiral crystals grow outside the silica helical ribbons. This is in good agreement with the red shift observed with emission spectra, i.e. the broadening of the emission spectra originates from the emission of a larger size of achiral PNC growth outside the hollow silica ribbons.

In sum, the lower the evaporation temperature and the slower the evaporation speed, the higher the ratio of helical and chiral PNC with respect to the achiral crystal growth outside the silica helical ribbons showing higher G values.

We also verified that the observed CD and CPL signals are not due to the chiral scattering from silica helices.⁶¹ Silica helices and achiral quantum dots (QDs) were drop-casted on the same side (in contact) or opposite side (not in contact) of the quartz: no detectable CD and CPL were observed (Figure S8) confirming that the observed CD and CPL by the PNC inside the silica nanohelices do not originate from the chiral scattering of the silica helices.

The chiroptical properties were also observed from PNCs grown with the one-step method. 0.5 mL ion precursor solutions in DMF with a concentration (0.04 M, 23 mg/mL,

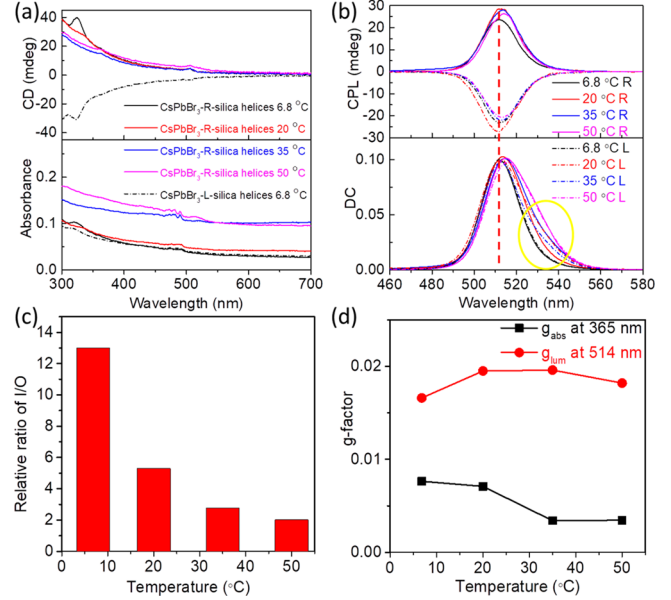


Figure 4. CD, absorption (a) and CPL, DC (b) spectra of CsPbBr₃-R/L-silica helices growth at different evaporation temperatures. Relative ratio of inside and outside PNCs (c) and g_{abs} , g_{gum} (d) of CsPbBr₃-R-silica helices growth at different evaporation temperatures and evaporation speeds. The relative ratio of inside and outside PNCs was calculated by the DC curves fitting (Figure S7). All CPL and DC spectra were measured under the irradiation of 365 nm excitation light.

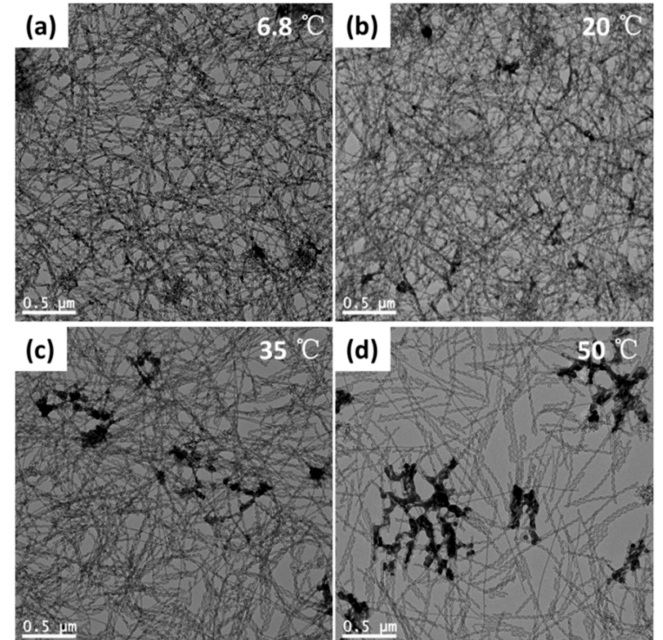


Figure 5. Lower magnification of TEM images of PNC growth at 6.8 °C (a), 20 °C (b), 35 °C (c), and 50 °C (d), respectively.

corresponding to 11.5 mg) were mixed with different amounts of silica helical ribbons: 0.5, 1.0, 1.5, 2.0 mg. This corresponds to Cs⁺Pb²⁺Br⁻/silica helices = 23, 11.5, 7.7, and 5.8. Then, 50 μL of each suspension was drop-casted on the surface of quartz slides (1 × 1 cm) and dried at room temperature. Similar helical domains with higher electron densities were observed as the ones obtained with the two-step method. CD and CPL

signals with slightly lower g-factors ($g_{abs} \sim 2 \times 10^{-3}$, $g_{lum} \sim 1 \times 10^{-2}$) were observed (Figure S9).

The effect of the replacement of Br^- by I^- was investigated. Here, the ion precursors were prepared by dispersing CsBr , CsI , PbBr_2 , and PbI_2 in DMF with different ratios of Br and I, keeping the stoichiometric ratio between $\text{Cs:Pb:Br:I} = 1:1:x:3-x$. The solution of mixed halide ion precursor (10 μL , 0.04 M), $x = 0, 0.75, 1.5$, was drop-casted on the surface of the 100 μg silica helices quartz substrate. Although the TEM images show a similar contrast increase of some of the silica helices (Figures S11(a-c)), while the dried sample showed strong CD signals (Figure S12, right- (left)-handed samples show positive (negative) signals), these samples were not emissive, and the absorption spectra show a blue shift to 420 nm which results from the yellow nonperovskite polymorph.^{66,67}

The H-PNCs (CsPbBr_3) have been successfully prepared by two supersaturated recrystallization methods assisted by the hollow silica ribbons. Both one-step and two-step methods show strong optical activities both for CD and CPL. The two-step method shows a larger g-factor and easier control of the ratio of silica and ion precursor with a dissymmetric g-factor up to 2×10^{-2} . Both the ratios of the silica ribbons and ion precursors and the solvent evaporation temperature show a significant effect on the PNC growth inside and outside the hollow silica ribbons which has a strong effect on the g_{lum} and g_{abs} . For the mixed halide ions (Br^- and I^-), a yellow nonperovskite type nanocrystal grows inside the hollow silica helical ribbons, which showed strong CD, while no emission was observed. The versatile and simple method to prepare the chiral shaped PNCs with high g-factors prepared inside the hollow silica ribbons would enrich the chiral group of PNCs for their further applications.

■ ASSOCIATED CONTENT

● Supporting Information

Detailed experimental conditions as well as characterization; additional figures describing the models of silica helical/twisted ribbons and their hollow volume calculations, SEM, SAED pattern of helical PNCs, photographs of PNCs@silica helical ribbons under room light and UV light at 365 nm, Photoluminescence and photoluminescence quantum yield of PNCs@silica helical ribbons, TCD, DRCD, CPL, g-factor of $\text{CsPbBr}_{x}\text{I}_{(1-x)}$ @silica helical/twisted ribbons (PDF)

■ AUTHOR INFORMATION

Corresponding Author

Reiko Oda – Univ. Bordeaux, CNRS, Bordeaux INP, CBMN, UMR 5248, 33600 Pessac, France; WPI-Advanced Institute for Materials Research, Tohoku University, 980-8577 Sendai, Japan; orcid.org/0000-0003-3273-8635; Email: reiko.oda@u-bordeaux.fr

Authors

Peizhao Liu – Univ. Bordeaux, CNRS, Bordeaux INP, CBMN, UMR 5248, 33600 Pessac, France; Graduate School of Energy Science, Kyoto University, 606-8501 Kyoto, Japan
Yann Battie – Université de Lorraine, Laboratoire de Chimie et Physique - Approche Multi-échelles des milieux Complexes,

(LCP-A2MC), 57078 Metz, France; orcid.org/0000-0003-2421-2684

Takaki Kimura – Graduate School of Energy Science, Kyoto University, 606-8501 Kyoto, Japan; orcid.org/0000-0003-1989-0149

Yutaka Okazaki – Graduate School of Energy Science, Kyoto University, 606-8501 Kyoto, Japan; orcid.org/0000-0003-2261-5914

Piyanan Pranee – Univ. Bordeaux, CNRS, Bordeaux INP, CBMN, UMR 5248, 33600 Pessac, France

Hao Wang – Univ. Bordeaux, CNRS, Bordeaux INP, CBMN, UMR 5248, 33600 Pessac, France

Emilie Pouget – Univ. Bordeaux, CNRS, Bordeaux INP, CBMN, UMR 5248, 33600 Pessac, France; orcid.org/0000-0002-3175-6201

Sylvain Nlate – Univ. Bordeaux, CNRS, Bordeaux INP, CBMN, UMR 5248, 33600 Pessac, France

Takashi Sagawa – Graduate School of Energy Science, Kyoto University, 606-8501 Kyoto, Japan; orcid.org/0000-0002-0908-0487

Complete contact information is available at:

Author Contributions

The manuscript was written through contributions of all authors. All authors have given approval to the final version of the manuscript.

Notes

The authors declare no competing financial interest.

■ ACKNOWLEDGMENTS

This work was supported by the France-Japan International Associated Laboratory, Chiral Nanostructures for Photonic Applications (LIA_CNPA_RO_R175_UBx-DRI DAJ DIRVED) as well as the Centre National de la Recherche Scientifique and Université de Bordeaux. Y.O. acknowledges the JSPS Overseas Research Fellowship. P.L. and H.W. are grateful for financial support from the Chinese Scholarship Council (CSC). P.L. thanks CNRS for the fellowship.

■ REFERENCES

- (1) Shi, D.; Adinolfi, V.; Comin, R.; Yuan, M.; Alarousu, E.; Buin, A.; Chen, Y.; Hoogland, S.; Rothenberger, A.; Katsiev, K.; et al. Solar cells. Low trap-state density and long carrier diffusion in organolead trihalide perovskite single crystals. *Science* **2015**, *347* (6221), 519–522.
- (2) Dong, Q.; Fang, Y.; Shao, Y.; Mulligan, P.; Qiu, J.; Cao, L.; Huang, J. Solar cells. Electron-hole diffusion lengths > 175 μm in solution-grown $\text{CH}_3\text{NH}_3\text{PbI}_3$ single crystals. *Science* **2015**, *347* (6225), 967–970.
- (3) Kim, J. Y.; Lee, J. W.; Jung, H. S.; Shin, H.; Park, N. G. High-Efficiency Perovskite Solar Cells. *Chem. Rev.* **2020**, *120* (15), 7867–7918.
- (4) Du, P.; Gao, L.; Tang, J. Focus on performance of perovskite light-emitting diodes. *Frontiers of Optoelectronics* **2020**, *13* (3), 235–245.
- (5) Chen, W.; Zhang, S.; Zhou, M.; Zhao, T.; Qin, X.; Liu, X.; Liu, M.; Duan, P. Two-Photon Absorption-Based Upconverted Circularly Polarized Luminescence Generated in Chiral Perovskite Nanocrystals. *J. Phys. Chem. Lett.* **2019**, *10* (12), 3290–3295.
- (6) Yuan, C.; Li, X.; Semin, S.; Feng, Y.; Rasing, T.; Xu, J. Chiral Lead Halide Perovskite Nanowires for Second-Order Nonlinear Optics. *Nano Lett.* **2018**, *18* (9), 5411–5417.

- (7) Naciri, J.; Shenoy, D. K.; Keller, P.; Gray, S.; Crandall, K.; Shashidhar, R. Synthesis and Pyroelectric Properties of Novel Ferroelectric Organosiloxane Liquid Crystalline Materials. *Chem. Mater.* **2002**, *14* (12), 5134–5139.
- (8) Zhang, H. Y.; Tang, Y. Y.; Shi, P. P.; Xiong, R. G. Toward the Targeted Design of Molecular Ferroelectrics: Modifying Molecular Symmetries and Homochirality. *Acc. Chem. Res.* **2019**, *52* (7), 1928–1938.
- (9) Sanchez, D. S.; Belopolski, I.; Cochran, T. A.; Xu, X.; Yin, J. X.; Chang, G.; Xie, W.; Manna, K.; Suss, V.; Huang, C. Y.; et al. Topological chiral crystals with helicoid-arc quantum states. *Nature* **2019**, *567* (7749), 500–505.
- (10) Chen, C.; Gao, L.; Gao, W.; Ge, C.; Du, X.; Li, Z.; Yang, Y.; Niu, G.; Tang, J. Circularly polarized light detection using chiral hybrid perovskite. *Nat. Commun.* **2019**, *10* (1), 1927.
- (11) Kim, Y. H.; Zhai, Y.; Lu, H.; Pan, X.; Xiao, C.; Gaulding, E. A.; Harvey, S. P.; Berry, J. J.; Vardeny, Z. V.; Luther, J. M.; et al. Chiral-induced spin selectivity enables a room-temperature spin light-emitting diode. *Science* **2021**, *371* (6534), 1129–1133.
- (12) Bisoyi, H. K.; Li, Q. Light-Directing Chiral Liquid Crystal Nanostructures: From 1D to 3D. *Acc. Chem. Res.* **2014**, *47* (10), 3184–3195.
- (13) Service, R. F. Ultrafast Lasers. Lighting the Way to a Quantum Computer. *Science* **2001**, *292* (5526), 2412–2413.
- (14) Humphreys, P. C.; Kalb, N.; Morits, J. P. J.; Schouten, R. N.; Vermeulen, R. F. L.; Twitchen, D. J.; Markham, M.; Hanson, R. Deterministic delivery of remote entanglement on a quantum network. *Nature* **2018**, *558* (7709), 268–273.
- (15) Michaeli, K.; Kantor-Urieli, N.; Naaman, R.; Waldeck, D. H. The electron's spin and molecular chirality - how are they related and how do they affect life processes? *Chem. Soc. Rev.* **2016**, *45* (23), 6478–6487.
- (16) Long, G.; Sabatini, R.; Saidaminov, M. I.; Lakhwani, G.; Rasmita, A.; Liu, X.; Sargent, E. H.; Gao, W. Chiral-perovskite optoelectronics. *Nature Reviews Materials* **2020**, *5* (6), 423–439.
- (17) Naaman, R.; Paltiel, Y.; Waldeck, D. H. Chiral Induced Spin Selectivity Gives a New Twist on Spin-Control in Chemistry. *Acc. Chem. Res.* **2020**, *53* (11), 2659–2667.
- (18) Naaman, R.; Waldeck, D. H. Chiral-Induced Spin Selectivity Effect. *J. Phys. Chem. Lett.* **2012**, *3* (16), 2178–2187.
- (19) Abendroth, J. M.; Stemer, D. M.; Bloom, B. P.; Roy, P.; Naaman, R.; Waldeck, D. H.; Weiss, P. S.; Mondal, P. C. Spin Selectivity in Photoinduced Charge-Transfer Mediated by Chiral Molecules. *ACS Nano* **2019**, *13* (5), 4928–4946.
- (20) Dang, Y.; Liu, X.; Cao, B.; Tao, X. J. M. Chiral halide perovskite crystals for optoelectronic applications. *Matter* **2021**, *4* (3), 794–820.
- (21) Ma, J.; Wang, H.; Li, D. Recent Progress of Chiral Perovskites: Materials, Synthesis, and Properties. *Adv. Mater.* **2021**, *33*, 2008785.
- (22) Dong, Y.; Zhang, Y.; Li, X.; Feng, Y.; Zhang, H.; Xu, J. Chiral Perovskites: Promising Materials toward Next-Generation Optoelectronics. *Small* **2019**, *15* (39), 1902237.
- (23) Kuznetsova, V. A.; Mates-Torres, E.; Prochukhan, N.; Marcaste, M.; Purcell-Milton, F.; O'Brien, J.; Visheratina, A. K.; Martinez-Carmona, M.; Grornova, Y.; Garcia-Melchor, M.; et al. Effect of Chiral Ligand Concentration and Binding Mode on Chiroptical Activity of CdSe/CdS Quantum Dots. *ACS Nano* **2019**, *13* (11), 13560–13572.
- (24) Gao, X.; Zhang, X.; Deng, K.; Han, B.; Zhao, L.; Wu, M.; Shi, L.; Lv, J.; Tang, Z. Excitonic Circular Dichroism of Chiral Quantum Rods. *J. Am. Chem. Soc.* **2017**, *139* (25), 8734–8739.
- (25) Gao, X.; Zhang, X.; Zhao, L.; Huang, P.; Han, B.; Lv, J.; Qiu, X.; Wei, S. H.; Tang, Z. Distinct Excitonic Circular Dichroism between Wurtzite and Zincblende CdSe Nanoplatelets. *Nano Lett.* **2018**, *18* (11), 6665–6671.
- (26) Liu, P.; Battie, Y.; Decossas, M.; Tan, S.; Pouget, E.; Okazaki, Y.; Sagawa, T.; Oda, R. Chirality Induction to CdSe Nanocrystals Self-Organized on Silica Nanohelices: Tuning Chiroptical Properties. *ACS Nano* **2021**, *15*, 16411.
- (27) Liu, P.; Chen, W.; Okazaki, Y.; Battie, Y.; Brocard, L.; Decossas, M.; Pouget, E.; Muller-Buschbaum, P.; Kauffmann, B.; Pathan, S.; et al. Optically Active Perovskite CsPbBr₃ Nanocrystals Helically Arranged on Inorganic Silica Nanohelices. *Nano Lett.* **2020**, *20* (12), 8453–8460.
- (28) Shi, Y.; Duan, P.; Huo, S.; Li, Y.; Liu, M. Endowing Perovskite Nanocrystals with Circularly Polarized Luminescence. *Adv. Mater.* **2018**, *30* (12), 1705011.
- (29) Ben-Moshe, A.; Govorov, A. O.; Markovich, G. Enantioselective synthesis of intrinsically chiral mercury sulfide nanocrystals. *Angew. Chem., Int. Ed. Engl.* **2013**, *52* (4), 1275–1279.
- (30) Flack, H. D. Chiral and Achiral Crystal Structures. *Helv. Chim. Acta* **2003**, *86* (4), 905–921.
- (31) Wang, P. P.; Yu, S. J.; Ouyang, M. Assembled Suprastructures of Inorganic Chiral Nanocrystals and Hierarchical Chirality. *J. Am. Chem. Soc.* **2017**, *139* (17), 6070–6073.
- (32) Ben-Moshe, A.; Wolf, S. G.; Bar Sadan, M.; Houben, L.; Fan, Z.; Govorov, A. O.; Markovich, G. Enantioselective control of lattice and shape chirality in inorganic nanostructures using chiral biomolecules. *Nat. Commun.* **2014**, *5*, 4302.
- (33) Wang, P. P.; Yu, S. J.; Govorov, A. O.; Ouyang, M. Cooperative expression of atomic chirality in inorganic nanostructures. *Nat. Commun.* **2017**, *8*, 14312.
- (34) Orme, C. A.; Noy, A.; Wierzbicki, A.; McBride, M. T.; Grantham, M.; Teng, H. H.; Dove, P. M.; DeYoreo, J. J. Formation of chiral morphologies through selective binding of amino acids to calcite surface steps. *Nature* **2001**, *411* (6839), 775–779.
- (35) Lee, H. E.; Ahn, H. Y.; Mun, J.; Lee, Y. Y.; Kim, M.; Cho, N. H.; Chang, K.; Kim, W. S.; Rho, J.; Nam, K. T. Amino-acid- and peptide-directed synthesis of chiral plasmonic gold nanoparticles. *Nature* **2018**, *556* (7701), 360–365.
- (36) Duan, Y.; Liu, X.; Han, L.; Asahina, S.; Xu, D.; Cao, Y.; Yao, Y.; Che, S. Optically active chiral CuO "nanoflowers". *J. Am. Chem. Soc.* **2014**, *136* (20), 7193–7196.
- (37) Hazen, R. M.; Sholl, D. S. Chiral selection on inorganic crystalline surfaces. *Nat. Mater.* **2003**, *2* (6), 367–374.
- (38) Ernst, K.-H. Molecular chirality in surface science. *Surf. Sci.* **2013**, *613*, 1–5.
- (39) Meng, F.; Morin, S. A.; Forticaux, A.; Jin, S. Screw dislocation driven growth of nanomaterials. *Acc. Chem. Res.* **2013**, *46* (7), 1616–1626.
- (40) Shtukenberg, A. G.; Punin, Y. O.; Gujral, A.; Kahr, B. Growth actuated bending and twisting of single crystals. *Angew. Chem., Int. Ed. Engl.* **2014**, *53* (3), 672–699.
- (41) Liu, Y.; Wang, J.; Kim, S.; Sun, H.; Yang, F.; Fang, Z.; Tamura, N.; Zhang, R.; Song, X.; Wen, J.; et al. Helical van der Waals crystals with discretized Eshelby twist. *Nature* **2019**, *570* (7761), 358–362.
- (42) Ben-Moshe, A.; da Silva, A.; Muller, A.; Abu-Odeh, A.; Harrison, P.; Waelder, J.; Niroui, F.; Ophus, C.; Minor, A. M.; Asta, M.; et al. The chain of chirality transfer in tellurium nanocrystals. *Science* **2021**, *372* (6543), 729–733.
- (43) Bierman, M. J.; Lau, Y. K.; Kvist, A. V.; Schmitt, A. L.; Jin, S. Dislocation-driven nanowire growth and Eshelby twist. *Science* **2008**, *320* (5879), 1060–1063.
- (44) Parala, H.; Winkler, H.; Kolbe, M.; Wohlfart, A.; Fischer, R. A.; Schmeichel, R.; Seggern, H. v. Confinement of CdSe Nanoparticles Inside MCM-41. *Adv. Mater.* **2000**, *12* (14), 1050–1055.
- (45) Li, Y.; Xu, D.; Zhang, Q.; Chen, D.; Huang, F.; Xu, Y.; Guo, G.; Gu, Z. Preparation of Cadmium Sulfide Nanowire Arrays in Anodic Aluminum Oxide Templates. *Chem. Mater.* **1999**, *11* (12), 3433–3435.
- (46) Hirai, T.; Okubo, H.; Komatsuwa, I. Size-Selective Incorporation of CdS Nanoparticles into Mesoporous Silica. *J. Phys. Chem. B* **1999**, *103* (21), 4228–4230.
- (47) Agger, J. R.; Anderson, M. W.; Pemble, M. E.; Terasaki, O.; Nozue, Y. Growth of Quantum-Confining Indium Phosphide inside MCM-41. *J. Phys. Chem. B* **1998**, *102* (18), 3345–3353.

- (48) Lu, A. H.; Schüth, F. Nanocasting: A Versatile Strategy for Creating Nanostructured Porous Materials. *Adv. Mater.* **2006**, *18* (14), 1793–1805.
- (49) Martin, C. R. Nanomaterials: a membrane-based synthetic approach. *Science* **1994**, *266* (5193), 1961–1966.
- (50) Zhang, L.; Jin, L.; Liu, B.; He, J. Templatized Growth of Crystalline Mesoporous Materials: From Soft/Hard Templates to Colloidal Templates. *Front Chem.* **2019**, *7*, 22.
- (51) Longo, G.; Pertegás, A.; Martínez-Sarti, L.; Sessolo, M.; Bolink, H. J. Highly luminescent perovskite–aluminum oxide composites. *Journal of Materials Chemistry C* **2015**, *3* (43), 11286–11289.
- (52) Zhang, Q.; Wang, B.; Zheng, W.; Kong, L.; Wan, Q.; Zhang, C.; Li, Z.; Cao, X.; Liu, M.; Li, L. Ceramic-like stable CsPbBr₃ nanocrystals encapsulated in silica derived from molecular sieve templates. *Nat. Commun.* **2020**, *11* (1), 31.
- (53) Dirin, D. N.; Protesescu, L.; Trummer, D.; Kochetygov, I. V.; Yakunin, S.; Krumeich, F.; Stadie, N. P.; Kovalenko, M. V. Harnessing Defect-Tolerance at the Nanoscale: Highly Luminescent Lead Halide Perovskite Nanocrystals in Mesoporous Silica Matrixes. *Nano Lett.* **2016**, *16* (9), 5866–5874.
- (54) Zong, Y.; Yang, T.; Hao, P.; Shan, B.; Peng, B.; Hu, X.; Tao, R.; Chen, X.; Wu, P.; Zhang, K. Spatial and chemical confined ultra-small CsPbBr₃ perovskites in dendritic mesoporous silica nanospheres with enhanced stability. *Microporous Mesoporous Mater.* **2020**, *302*, 110229.
- (55) Liu, P.; Chen, W.; Wang, W.; Xu, B.; Wu, D.; Hao, J.; Cao, W.; Fang, F.; Li, Y.; Zeng, Y.; et al. Halide-Rich Synthesized Cesium Lead Bromide Perovskite Nanocrystals for Light-Emitting Diodes with Improved Performance. *Chem. Mater.* **2017**, *29* (12), 5168–5173.
- (56) Oda, R.; Huc, I.; Schmutz, M.; Candau, S.; MacKintosh, F. Tuning bilayer twist using chiral counterions. *Nature* **1999**, *399* (6736), 566–569.
- (57) Brizard, A.; Aimé, C.; Labrot, T.; Huc, I.; Berthier, D.; Artzner, F.; Desbat, B.; Oda, R. Counterion, temperature, and time modulation of nanometric chiral ribbons from gemini-tartrate amphiphiles. *J. Am. Chem. Soc.* **2007**, *129* (12), 3754–3762.
- (58) Sugiyasu, K.; Tamaru, S.-i.; Takeuchi, M.; Berthier, D.; Huc, I.; Oda, R.; Shinkai, S. Double helical silica fibrils by sol–gel transcription of chiral aggregates of gemini surfactants. *Chem. Commun.* **2002**, No. 11, 1212–1213.
- (59) Delclos, T.; Aime, C.; Pouget, E.; Brizard, A.; Huc, I.; Delville, M. H.; Oda, R. Individualized silica nanohelices and nanotubes: tuning inorganic nanostructures using lipidic self-assemblies. *Nano Lett.* **2008**, *8* (7), 1929–1935.
- (60) Protesescu, L.; Yakunin, S.; Bodnarchuk, M. I.; Krieg, F.; Caputo, R.; Hendon, C. H.; Yang, R. X.; Walsh, A.; Kovalenko, M. V. Nanocrystals of Cesium Lead Halide Perovskites (CsPbX₃, X = Cl, Br, and I): Novel Optoelectronic Materials Showing Bright Emission with Wide Color Gamut. *Nano Lett.* **2015**, *15* (6), 3692–3696.
- (61) Liu, P.; Battie, Y.; Okazaki, Y.; Ryu, N.; Pouget, E.; Nlate, S.; Sagawa, T.; Oda, R. Chiral optical scattering from helical and twisted silica nanoribbons. *Chem. Commun. (Camb)* **2021**, *57* (90), 12024–12027.
- (62) Oda, R.; Artzner, F.; Laguerre, M.; Huc, I. Molecular Structure of Self-Assembled Chiral Nanoribbons and Nanotubules Revealed in the Hydrated State. *J. Am. Chem. Soc.* **2008**, *130* (44), 14705–14712.
- (63) Hohenester, U. Simulating electron energy loss spectroscopy with the MNPBEM toolbox. *Comput. Phys. Commun.* **2014**, *185* (3), 1177–1187.
- (64) Palik, E. D. *Handbook of Optical Constants of Solids*; Academic Press: 1998.
- (65) Yan, W.; Mao, L.; Zhao, P.; Mertens, A.; Dottermusch, S.; Hu, H.; Jin, Z.; Richards, B. S. Determination of complex optical constants and photovoltaic device design of all-inorganic CsPbBr₃ perovskite thin films. *Opt. Express* **2020**, *28* (10), 15706–15717.
- (66) Sutton, R. J.; Filip, M. R.; Haghimirad, A. A.; Sakai, N.; Wenger, B.; Giustino, F.; Snaith, H. J. Cubic or Orthorhombic? Revealing the Crystal Structure of Metastable Black-Phase CsPbI₃ by Theory and Experiment. *ACS Energy Letters* **2018**, *3* (8), 1787–1794.
- (67) Eperon, G. E.; Paternò, G. M.; Sutton, R. J.; Zampetti, A.; Haghimirad, A. A.; Cacialli, F.; Snaith, H. J. Inorganic caesium lead iodide perovskite solar cells. *Journal of Materials Chemistry A* **2015**, *3* (39), 19688–19695.

□ Recommended by ACS

Tunable Circular Photogalvanic and Photovoltaic Effect in 2D Tellurium with Different Chirality

Chang Niu, Peide D. Ye, et al.

APRIL 14, 2023

NANO LETTERS

READ ▶

Chirality-Dependent Structural Transformation in Chiral 2D Perovskites under High Pressure

Meng-En Sun, Shuang-Quan Zang, et al.

APRIL 14, 2023

JOURNAL OF THE AMERICAN CHEMICAL SOCIETY

READ ▶

Chirality Induction at the Helically Twisted Surface of Nanoparticles Generating Circularly Polarized Luminescence

Jumpei Kuno, Takuya Nakashima, et al.

OCTOBER 06, 2022

CHEMISTRY OF MATERIALS

READ ▶

Chain-to-Layer Dimensionality Engineering of Chiral Hybrid Perovskites to Realize Passive Highly Circular-Polarization-Sensitive Photodetection

Tingting Zhu, Junhua Luo, et al.

SEPTEMBER 23, 2022

JOURNAL OF THE AMERICAN CHEMICAL SOCIETY

READ ▶

Get More Suggestions >